Published in final edited form as:

IEEE Nucl Sci Symp Conf Rec (1997). 2008 October ; 2008: 5548–5551. doi:10.1109/NSSMIC.2008.4774505

Adaptive SPECT for Tumor Necrosis Detection

Luca Caucci,
College of Optical Sciences, University of Arizona, 1630 E. University Blvd., Tucson, Arizona. 85721 and also with the Center for Gamma-Ray Imaging, University of Arizona, 1609 N. Warren Ave., Tucson, Arizona 85719

Matthew A. Kupinski,
College of Optical Sciences, University of Arizona, 1630 E. University Blvd., Tucson, Arizona. 85721 and also with the Center for Gamma-Ray Imaging, University of Arizona, 1609 N. Warren Ave., Tucson, Arizona 85719

Melanie Freed,
U.S. Food and Drug Administration, 10903 New Hampshire Ave., Silver Spring, Maryland 20993

Lars R. Furenlid [Member, IEEE],
College of Optical Sciences, University of Arizona, 1630 E. University Blvd., Tucson, Arizona. 85721 and also with the Center for Gamma-Ray Imaging, University of Arizona, 1609 N. Warren Ave., Tucson, Arizona 85719

Donald W. Wilson, and
Center for Gamma-Ray Imaging, University of Arizona, 1609 N. Warren Ave., Tucson, Arizona 85719

Harrison H. Barrett [Fellow, IEEE]
College of Optical Sciences, University of Arizona, 1630 E. University Blvd., Tucson, Arizona. 85721 and also with the Center for Gamma-Ray Imaging, University of Arizona, 1609 N. Warren Ave., Tucson, Arizona 85719

Abstract

In this paper, we consider a prototype of an adaptive SPECT system, and we use simulation to objectively assess the system's performance with respect to a conventional, non-adaptive SPECT system. Objective performance assessment is investigated for a clinically relevant task: the detection of tumor necrosis at a known location and in a random lumpy background. The iterative maximum-likelihood expectation-maximization (MLEM) algorithm is used to perform image reconstruction. We carried out human observer studies on the reconstructed images and compared the probability of correct detection when the data are generated with the adaptive system as opposed to the non-adaptive system. Task performance is also assessed by using a channelized Hotelling observer, and the area under the receiver operating characteristic curve is the figure of merit for the detection task. Our results show a large performance improvement of adaptive systems versus non-adaptive systems and motivate further research in adaptive medical imaging.

Index Term

SPECT; adaptive imaging; multimodality imaging; tumor necrosis; assessment of image quality; human observer; detection; channelized Hotelling observer; MLEM reconstruction; ROC curve

I. Introduction

Traditional SPECT systems have a fixed geometry which implies that the same configuration is used to image different organs in different patients to perform different tasks. These systems are not generally optimized for a particular task and, because they cannot reconfigure themselves, it is not possible to obtain high performance and image quality on a wide variety of tasks and objects of interest. On the other hand, adaptive systems can be optimized for a wide range of tasks. We can consider systems in which a low-resolution pre-scan is used to learn something about the object, and then the system's configuration is adjusted based on such information. Final data are then acquired using the reconfigured system. The pre-scan and the final scan can also be performed with two different modalities (for example, SPECT for the pre-scan and CT for the final scan). A mathematical framework for adaptive imaging has recently been published [1], [2], and a prototype of a SPECT adaptive system has been proposed as well [3]–[5].

In this work, we simulate the adaptive system of [3]–[5], and we use the reconstructed data to perform detection of necrosis in a tumor at a known location and in a random lumpy background. Detection performance is investigated by means of human studies and a computer model. In the human studies, a human observer is randomly shown reconstructed noisy images under both pathologies (necrosis present vs. necrosis absent), and he/she is to select the images that most likely correspond to the necrotic tumor. Such a process, if repeated for a large data set, gives the probability of correct classification for that particular human observer. The same experiment is usually repeated for many different human observers. In the case of a computer model, features are extracted from the reconstructed images, and the channelized Hotelling observer is used to perform a feature-based detection. A receiver operating characteristic curve is obtained.

In this study, human and model performance are computed for a non-adapted version of the imaging system as well: the comparison of task performance for the adapted and non-adapted systems shows a large improvement in terms of detection performance when adaptation is used.

II. Imaging with Adaptive Systems

A generic continuous-to-discrete imaging system can be described mathematically as $\boldsymbol{g} = \mathscr{H}f + \boldsymbol{n}$, in which $\boldsymbol{g} \in \mathbb{R}^M$ is the acquired data, $\mathscr{H}$ is the system operator, f is the real continuous object, and $\boldsymbol{n} \in \mathbb{R}^M$ is the random noise [6]. In many applications, reconstruction algorithms are run on the data $\boldsymbol{g}$ to obtain a vector $\hat{\boldsymbol{f}} \in \mathbb{R}^N$ that, in some sense, represent as closely as possible the real object f. The components of $\hat{\boldsymbol{f}}$ will be denoted as $\hat{\boldsymbol{f}}_n$, for $n = 1, \ldots, N$.

In an adaptive system, we have a pre-scan during which something is learned about the object. The system is then reconfigured, and the actual clinical scan is performed. We can think of a system operator for the clinical scan that either depends on the pre-scan data $\boldsymbol{g}_{\text{pre}}$ directly or via the reconstructed object $\hat{\boldsymbol{f}}_{\text{pre}}$ computed from $\boldsymbol{g}_{\text{pre}}$. For the first case, we can write:

$$\boldsymbol{g}_{\text{pre}}=\mathscr{H}_{\text{pre}}f+\boldsymbol{n}_{\text{pre}}, \quad \text{(1a)}$$

$$\boldsymbol{g}=\mathscr{H}(\boldsymbol{g}_{\text{pre}})f+\boldsymbol{n}, \quad \text{(1b)}$$

and, for the second case, we have:

$$\boldsymbol{g}_{\text{pre}}=\mathscr{H}_{\text{pre}}f+\boldsymbol{n}_{\text{pre}}, \quad \text{(1a)}$$

$$\boldsymbol{g}=\mathscr{H}(\hat{\boldsymbol{f}}_{\text{pre}})f+\boldsymbol{n}. \quad \text{(1b′)}$$

Details of the adaptive SPECT system we are considering are reported in [3], [4] and will not be repeated here. In this work, we assume that a region of interest (ROI) is confined during the pre-scan and subsequent post-processing, and that, as in [3], the system reconfigures itself in such a way that the ROI fills the detector as much as possible. Reconstruction of the noisy data is performed using the MLEM iterative algorithm:

$$\hat{f}_n^{(k+1)}=\hat{f}_n^{(k)}\left\{\frac{1}{\sum_{m=1}^{M}H_{mn}}\sum_{m=1}^{M}\frac{g_m H_{mn}}{\left[H\hat{\boldsymbol{f}}^{(k)}\right]_m}\right\}, \quad (2)$$

in which $H = [H_{mn}] \in \mathbb{R}^{M\times N}$ is a matrix that represents a discretized version of the system operator, the superscript k denotes the iteration number, and $n = 1, \ldots, N$ is the pixel index in the reconstructed image $\hat{\boldsymbol{f}}^{(k+1)}$.

Based on the promising results of previous tests and simulations [1], we decided to use the same system and same adaptation rule to perform tumor necrosis detection. The task of interest was the detection of necrosis in a tumor at a known location and buried in a random lumpy background. Detection of tumor necrosis is a relevant task in the field of oncology, because treatment/surgical procedures usually depend on the type of tumor. Optimal detectors for necrosis detection have been developed and their effectiveness analyzed by means of human studies [7]. To our knowledge, research on adaptive systems and adaptation rules for the same task are just being developed [1], [3].

Fig. 1(a) shows an example of a real PET image of a metastatic colorectal carcinoma in which tumor necrosis is not present. The same patient was imaged again about one year later, and the image of the same area is reported in Fig. 1(b): tumor necrosis has developed, and the carcinoma has spread as a new lymph-node metastasis.

For this research, we decided to use simulated data, and we simulated tumors located at a given location. For the case of a necrotic tumor, the density $D(\boldsymbol{r})$ of the tumoral area varied as shown in (3) on page 3. Lumpy background [8] was added to the simulated 3-D tumor described by $D(\boldsymbol{r})$ to get a simulated object that resembles as much as possible real images, as the ones shown in Fig. 1.

$$D(\boldsymbol{r})=\begin{cases} 0 & \text{if} |\boldsymbol{r}|>R, \\ \frac{m_1}{2}\left[1+\cos\left(\pi\frac{|\boldsymbol{r}|-R+S}{S}\right)\right] & \text{if} R-S<|\boldsymbol{r}|\leq R, \\ m_1 & \text{if} R-S-P<|\boldsymbol{r}|\leq R-S, \\ m_2+(m_1-m_2)\left[1+\cos\left(\pi+\frac{\pi}{2}\frac{|\boldsymbol{r}|}{R-S-P}\right)\right] & \text{if} |\boldsymbol{r}|\leq R-S-P. \end{cases} \quad (3)$$

The simulated object was passed through the adaptive system according to (1), and the data were reconstructed according to (2). Figs. 2(a) and 2(b) show the central part of slices of reconstructed 3-D simulated data when adaptation was used. The object being simulated contained tumor necrosis only in the case of Fig. 2(a), and visual examination of Figs. 2(a) and 2(b) shows that the adaptive system produced good images for necrosis detection. Figs. 2(c) and 2(d) show the same reconstructed data but when no adaptation was used. Although tumor necrosis is present in Fig. 2(c) only, the two slices look the same, and necrosis detection is impossible.

III. The Channelized Hotelling Observer

The channelized Hotelling observer (CHO) [9], [10] is a model observer that has been used extensively in the field of medical radiology for the assessment of image quality [6]. A schematic representation of the CHO is shown in Fig. 3. The input data $\hat{\boldsymbol{f}}$ (usually of very large size) are passed through a bank of K channels $\mathscr{C}_1, \ldots, \mathscr{C}_K$ The outputs, a set $\boldsymbol{\upsilon} = \{\upsilon_1, \ldots, \upsilon_K\} = \mathscr{C}(\hat{\boldsymbol{f}})$ of numbers called features, are supplied to the Hotelling observer [6], [11]. The Hotelling observer is a linear observer for a detection task, and is the optimal linear observer for the data vector $\boldsymbol{\upsilon}$. The output $t_{\mathrm{CHO}}(\hat{\boldsymbol{f}}) = t_{\mathrm{Hot}}[\mathscr{C}(\hat{\boldsymbol{f}})]$ of the CHO is compared to a threshold τ to make a decision: if $t_{\mathrm{CHO}}(\hat{\boldsymbol{f}}) > \tau$, the observer concludes that necrosis is present. Otherwise, no necrosis is assumed. Probabilities, such as the probability of a false alarm or the probability of a correct detection, can be estimated for different values of τ and such information can be summarized as a receiver operating characteristic (ROC) curve [12]–[14]. A meaningful figure of merit for the task is the area under the ROC curve (AUC) [6], [14], which is used here to assess system performance.

The channels we used in this study are the square filters (SQR) and the difference-of-Gaussians (DOG) [10]. These channels are called antrophomorphic in the sense that they approximate human channels for detection tasks. In the radial frequency domain, the SQR channels are defined as:

$$W_j(\boldsymbol{\rho})=\begin{cases} 0 & \text{if} |\boldsymbol{\rho}|\leq \rho_0\alpha^{j-1}, \\ 1 & \text{if} \rho_0\alpha^{j-1}<|\boldsymbol{\rho}|\leq \rho_0\alpha^{j}, \\ 0 & \text{if} |\boldsymbol{\rho}|>\rho_0\alpha^{j}. \end{cases} \quad (4)$$

The DOG channels are defined by:

$$W_j(\boldsymbol{\rho})=\exp\left\{-\frac{1}{2}\left(\frac{|\boldsymbol{\rho}|}{Q\sigma_0\alpha^j}\right)^2\right\}-\exp\left\{-\frac{1}{2}\left(\frac{|\boldsymbol{\rho}|}{\sigma_0\alpha^j}\right)^2\right\}. \quad (5)$$

The inverse Fourier transforms $w_j(\boldsymbol{r})$ of the functions $W_j(\boldsymbol{\rho})$ were computed analytically. The functions $w_j(\boldsymbol{r})$ were sampled on a 3-D pixel grid, and these sets of samples were raster-scanned to obtain vectors $\boldsymbol{w}_j$ The channel $\mathscr{C}_j$ was then defined as $\mathscr{C}_j(\hat{\boldsymbol{f}})=\boldsymbol{w}_j^\top\hat{\boldsymbol{f}}$ [10], where the symbol "⊤" denotes the transpose of a vector. Thus, the number $v_j=\boldsymbol{w}_j^\top\hat{\boldsymbol{f}}$ is the j-th channel bank output, as Fig. 3 shows.

We used the following parameters for the DOG channels: j = 1, …, 10, Q = 2, σ_0 = 0.01, and α = 1.50. For the SQR channels, we used j = 1, …, 6, ρ_0 = 0.015, and α = 1.50. Using the adaptive system, we simulated and reconstructed 1000 data sets for the case "necrosis not present" (hypothesis H_0) and 1000 data sets for the case "necrosis present" (hypothesis H_1). All reconstructions were run according to (2) for 20 iterations; for simplicity, we will drop the iteration index k we used in (2) and we will let $\hat{\boldsymbol{f}}$ denote the reconstructed data $\hat{\boldsymbol{f}}^{(20)}$ at the end of the 20th iteration. From the channel outputs $\boldsymbol{\upsilon}=\mathscr{C}(\hat{\boldsymbol{f}})$ and varying $\hat{\boldsymbol{f}}$ over the set of reconstructed data, it is possible to estimate by sample averaging the mean channel output vector $\bar{\boldsymbol{\upsilon}}_0$ under the hypothesis H_0 and, likewise, the mean channel output vector $\bar{\boldsymbol{\upsilon}}_1$ under the hypothesis H_1. Similarly, we can estimate the covariance matrices $\mathbf{K}_{\boldsymbol{\upsilon}_0}$ and $\mathbf{K}_{\boldsymbol{\upsilon}_1}$ of $\boldsymbol{\upsilon}$ under the hypotheses H_0 and H_1 respectively. It should be emphasized that the vectors $\bar{\boldsymbol{\upsilon}}_0$ and $\bar{\boldsymbol{\upsilon}}_1$ are of size $K \times 1$, and the matrices $\mathbf{K}_{\boldsymbol{\upsilon}_0}$ and $\mathbf{K}_{\boldsymbol{\upsilon}_1}$ are of size $K \times K$, where K is the number of channels (see Fig. 3). Usually, $K \lesssim 10 \ll M$; therefore, handling these vectors and matrices is computationally not difficult. The covariance matrix $\mathbf{K}_{\boldsymbol{\upsilon}}$ of $\boldsymbol{\upsilon}$ is thus given by $\mathbf{K}_{\boldsymbol{\upsilon}} = \Pr(H_0)\,\mathbf{K}_{\boldsymbol{\upsilon}_0} + \Pr(H_1)\,\mathbf{K}_{\boldsymbol{\upsilon}_1}$, where $\Pr(H_i)$ is the probability of hypothesis H_i. These probabilities might be unknown; hence it is generally assumed that $\Pr(H_0) = \Pr(H_1) = ½$, which gives $\mathbf{K}_{\boldsymbol{\upsilon}} = ½\,[\mathbf{K}_{\boldsymbol{\upsilon}_0} + \mathbf{K}_{\boldsymbol{\upsilon}_1}]$. This expression is also valid when $\mathbf{K}_{\boldsymbol{\upsilon}_0} \approx \mathbf{K}_{\boldsymbol{\upsilon}_1}$ which happens when the statistics of $\boldsymbol{\upsilon}$ under the two hypotheses are very close to each other (for example, when necrosis is just developing). The CHO is defined as $t_{\mathrm{CHO}}(\hat{\boldsymbol{f}}) = \boldsymbol{z}^\top\boldsymbol{\upsilon}$ [6], [10], where $\boldsymbol{z}=\mathbf{K}_{\upsilon}^{-1}[\bar{\boldsymbol{\upsilon}}_1-\bar{\boldsymbol{\upsilon}}_0]$ is the template vector.

Values of the random variable t_{CHO} were computed as $t_{\mathrm{CHO}}(\hat{\boldsymbol{f}})$ for $\hat{\boldsymbol{f}}$ varying over the set of reconstructed data under each hypothesis. The values of t_{CHO} were collected and used to estimate the probability density functions $\mathrm{pr}(t_{\mathrm{CHO}}|H_i)$ of the CHO test statistics under each hypothesis H_i and for both choices of the channel bank $\mathscr{C}$. Such densities are reported in Figs. 4(a) and 4(b). Intuitively, well-separated densities correspond to a low probability of misclassification. We repeated this analysis when the data were simulated with the non-adaptive system; the corresponding densities are reported in Figs. 4(c) and 4(d). From the values of t_{CHO}, it is possible to obtain ROC curves as well. We can define the false positive fraction (FPF) and the true positive fraction (TPF) as:

$$\mathrm{FPF}(\tau)=\Pr(t_{\mathrm{CHO}}>\tau|H_0),$$

$$\mathrm{TPF}(\tau)=\Pr(t_{\mathrm{CHO}}>\tau|H_1),$$

in which τ is a threshold, and the probabilities $\Pr(t_{\mathrm{CHO}} > \tau \mid H_i)$ are estimated from the data t_{CHO} under each hypothesis H_i, i = 0,1. Plotting TPF(τ) versus FPF(τ) as τ varies over the real line gives an ROC curve [6]. Comparisons between ROC curves for the adaptive and the non-adaptive systems and for the two choices of channel bank $\mathscr{C}$ are shown in Fig. 5.

Table I reports the values of the AUCs for the two different choices of the channel bank $\mathscr{C}$ and when the data were simulated with the adaptive system and the non-adaptive system. Because we used simulated noisy images to estimate the AUCs, the AUCs themselves are random variables. Therefore, we also estimated [15] the standard deviations σ on the AUCs (see Table I). From the AUC, the detectability d_A [6] is computed as $d_A = 2\ \mathrm{erf}^{-1}(2\ \mathrm{AUC} - 1)$, where $\mathrm{erf}(x)=2\pi^{-1/2}\int_0^x e^{-u^2}\mathrm{d}u$. The differences $\Delta d_A^2=\left(d_A^{\mathrm{adapt.}}\right)^2-\left(d_A^{\mathrm{non\text{-}\ adapt.}}\right)^2$ are meaningful measures for the increase in detection performance and are reported in the last column of Table I. Based on the values reported in Table I, we compute the *p*-values [16] on the AUCs, which are the probabilities of the events $\mathrm{AUC}_{\mathrm{DOG}}^{\mathrm{adapt.}} \leq \mathrm{AUC}_{\mathrm{DOG}}^{\mathrm{non\text{-}\ adapt.}}$ and $\mathrm{AUC}_{\mathrm{SQR}}^{\mathrm{adapt.}} \leq \mathrm{AUC}_{\mathrm{SQR}}^{\mathrm{non\text{-}\ adapt.}}$. Such probabilities turned out to be smaller than 10^{-100}, therefore, we can confidently state that the adaptive rule increases task performance. The Δd_A^2 column of Table I shows a large improvement in detection performance when adaptation was used and corroborates the empirical results of Fig. 2.

IV. Human Observer Studies

We have also carried out human studies in the form of two-alternative forced choice (2AFC) experiments. In a 2AFC setup, a human observer is randomly shown pairs of data sets, one in which the signal to be detected is present and the other where the signal is absent. The human observer is to identify the data set that contains the signal. This experiment is repeated many times for a large collection of pairs of data sets, and the answers are recorded. It can be proved [6] that the percentage of correct answers gives an estimate of the AUC for that particular observer. We considered 400 pairs of reconstructed data when the adaptive system was used and the same number of pairs of reconstructed data for the non-adaptive system case. We ran human studies with different observers, and we estimated the probabilities of correctly classifying the data set that contains the signal of interest. Results are reported in Table II. Further human studies are currently under way.

V. Conclusions

In this work, we considered an adaptive SPECT system, and we assessed its performance when the task of interest is the detection of tumor necrosis. We used simulation and applied a model observer, namely the channelized Hotelling observer, to the MLEM reconstructed data. We used two different choices of channel banks. We also considered human studies and carried out 2AFC experiments. We compared the adaptive system with the same system but when adaptation was switched off. The AUC and AUC-related detectability d_A were

used as figures-of-merit for the system. We estimated detection performance for both the adaptive and non-adaptive systems. Our results show that task performance improves when the adaptive system is used. This improvement was numerically quantified via the quantity Δd_A^2. These results corroborate the superiority of adaptive imaging systems with respect to non-adaptive imaging systems and encourage further research in the field of adaptive imaging for medical applications.

Acknowledgments

This work was supported by NIH grants P41EB002035 and R37EB000803.

References

1. Barrett HH, Furenlid LR, Freed M, Hesterman JY, Kupinski MA, Clarkson E, Whitaker MK. Adaptive SPECT. IEEE Trans. Med. lmag. 2008 Jun.27(6):775–788.
2. Clarkson E, Kupinski MA, Barrett HH, Furenlid LR. A task-based approach to adaptive and multimodality imaging. Proc. IEEE. 2008 Mar.96(3):500–511.
3. Freed M, Kupinski MA, Furenlid LR, Wilson DW, Barrett HH. A prototype instrument for single-photon small-animal adaptive SPECT imaging. Med. Phys. 2008 May; 35(5):1912–1925. [PubMed: 18561667]
4. Freed, M.; Kupinski, MA.; Furenlid, LR.; Whitaker, MK.; Barrett, HH. A prototype instrument for adaptive SPECT imaging. In: Hsieh, J.; Flynn, MJ., editors. Medical Imaging 2007: Physics of Medical Imaging. Vol. 6510. Proc. SPIE; 2007. p. 65100V
5. Freed, M.; Kupinski, MA.; Furenlid, LR.; Barrett, HH. Design of an adaptive SPECT imager; presented at the Acad. Molecular Imag. Annu. Conf.; Orlando, FL. 2006 Mar..
6. Barrett, HH.; Myers, KJ. Foundations of image Science. Hoboken, NJ: Wiley-Interscience; 2004.
7. Tsui BMW, Metz CE, Beck RN. Optimum detector spatial resolution for discriminating between tumour uptake distributions in scintigraphy. Phys. Med. Biol. 1983 Jul.28(7):775–788. [PubMed: 6611654]
8. Rolland JP, Barrett HH. Effect of random background in homogeneity on observer detection performance. J. Opt. Soc. Am. A. 1992 May; 9(5):649–658. [PubMed: 1588452]
9. Myers KJ, Barrett HH. Addition of a channel mechanism to the ideal-observer model. J. Opt. Soc. Am. A. 1987 Dec.4(12):2447–2457. [PubMed: 3430229]
10. Abbey CK, Barrett H. Human- and model-observer performance in ramp-spectrum noise: effects of regularization and object variability. J. Opt. Soc. Am. A. 2001 Mar.18(3):473–488.
11. Hotelling H. The generalization of Student's ratio. Ann. Math. Stat. 1931 Aug.2(3):360–378.
12. van Erkel AR, Pattynama PMT. Receiver operating characteristic (ROC) analysis: Basic principles and applications in radiology. Eur. J. Radiol. 1998; 27(2):88–94. [PubMed: 9639133]
13. Obuchowski NA. Receiver operating characteristic curves and their use in radiology. Radiology. 2003 Oct.229(1):3–8. [PubMed: 14519861]
14. Hanley A, McNeil BJ. The meaning and use of the area under a receiver operating characteristic (ROC) curve. Radiology. 1982 Apr.143(1):29–36. [PubMed: 7063747]
15. Gallas BD. One-shot estimate of MRMC variance: AUC. Acad. Radiol. 2006 Mar.13(3):353–362. [PubMed: 16488848]
16. Frieden, BR. Probability, Statistical Optics, and Data Testing. 3rd ed.. Berlin, Germany: Springer Verlag; 2001.

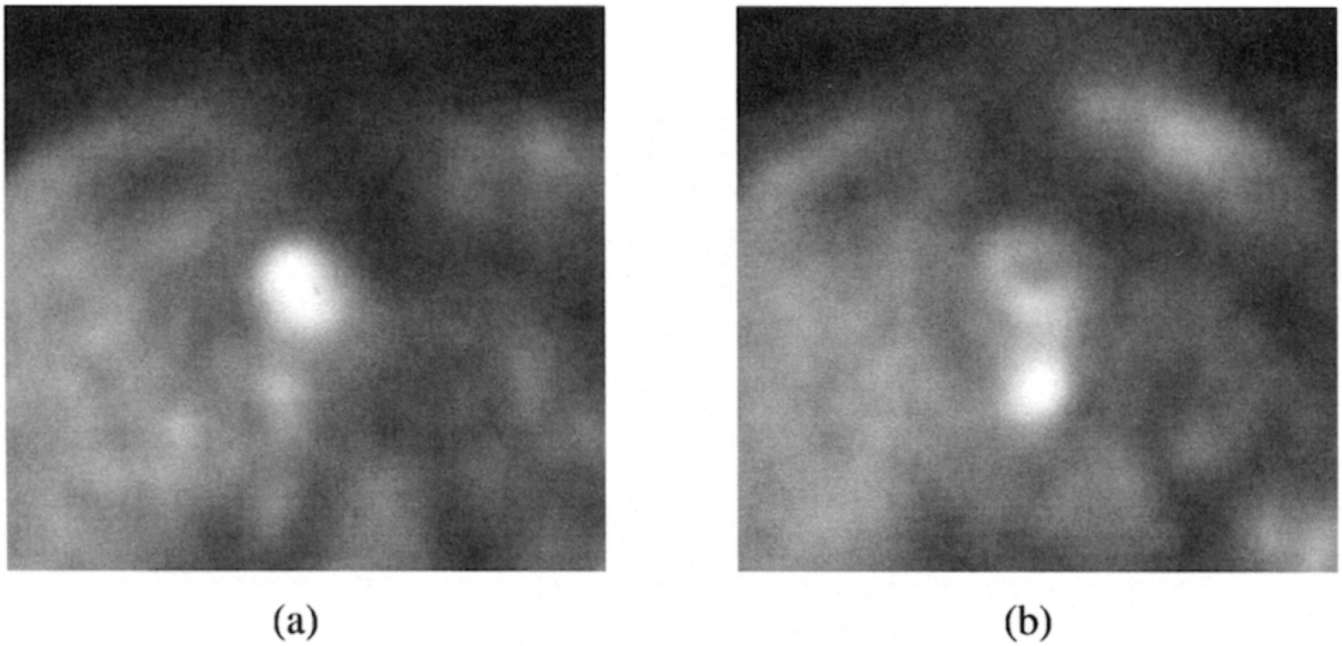

Fig. 1.

Clinical FDG PET transaxial images of a 77-year-old male with metastatic colorectal carcinoma. In (a), there is increased FDG uptake (spot near the center of the image) that represents metastasis to a lymph node adjacent to the liver. In (b), taken one year later, the previous focus of FDG uptake has decreased in intensity in the periphery, and the central region is now cold; this probably represents necrosis. In addition, there is a new lymph-node metastasis below the initial one. (Images courtesy of James M. Woolfenden.)

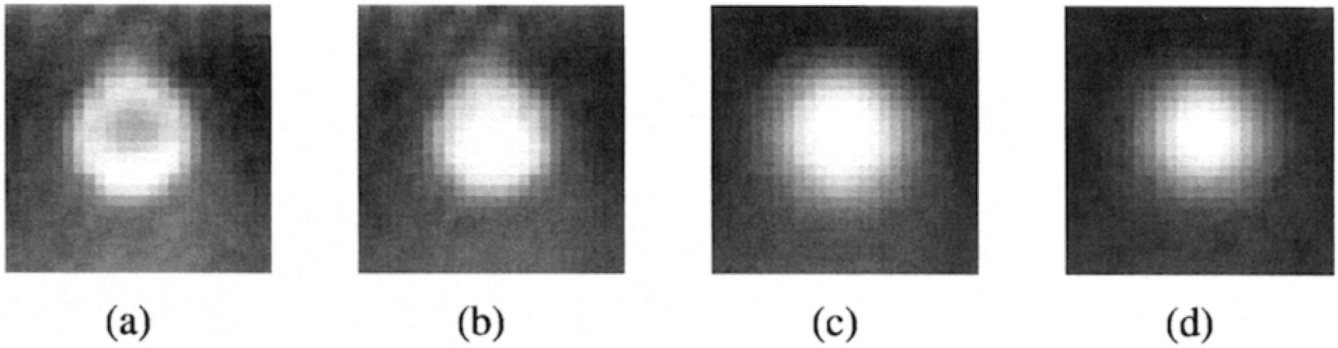

Fig. 2.

EM reconstruction of a simulated tumor. (a) and (b): data simulated with the adaptive system resulting in straightforward necrosis detection; (c) and (d): data simulated with the non-adaptive system resulting in much harder necrosis detection.

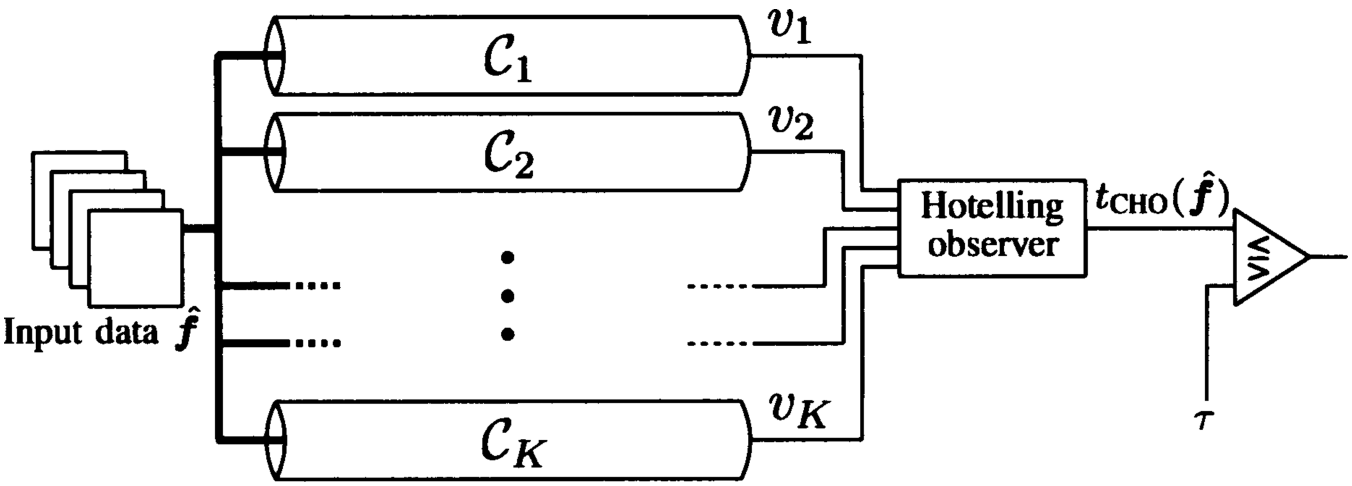

Fig. 3.
Schematic representation of the channelized Hotelling observer

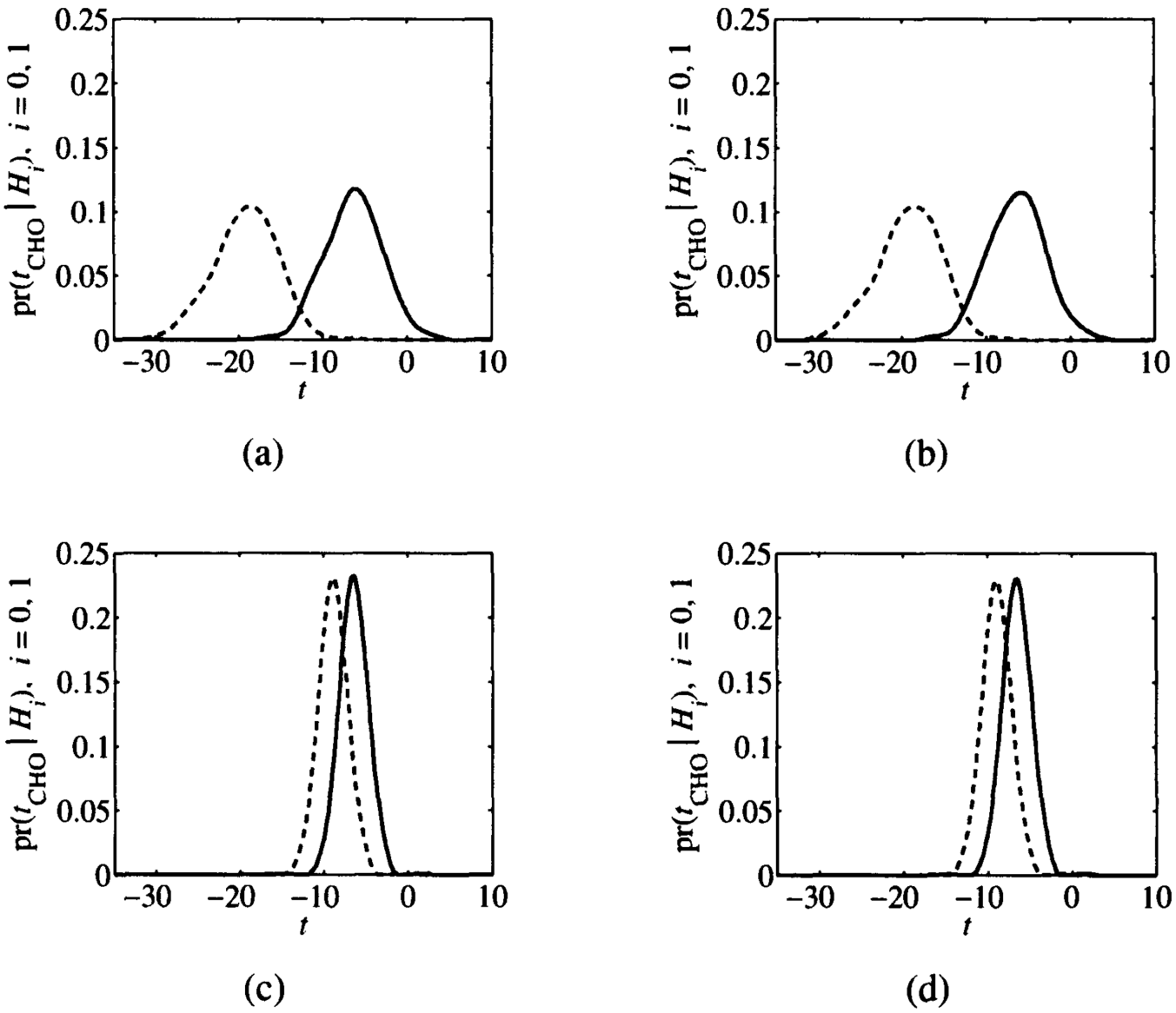

Fig. 4.

Estimated densities pr($t_{CHO}|H_i$), i = 0,1 for different cases. (a): DOG channels and adaptive system; (b): SQR channels and adaptive system; (c): DOG channels and non-adaptive system; (d): SQR channels and non-adaptive system.

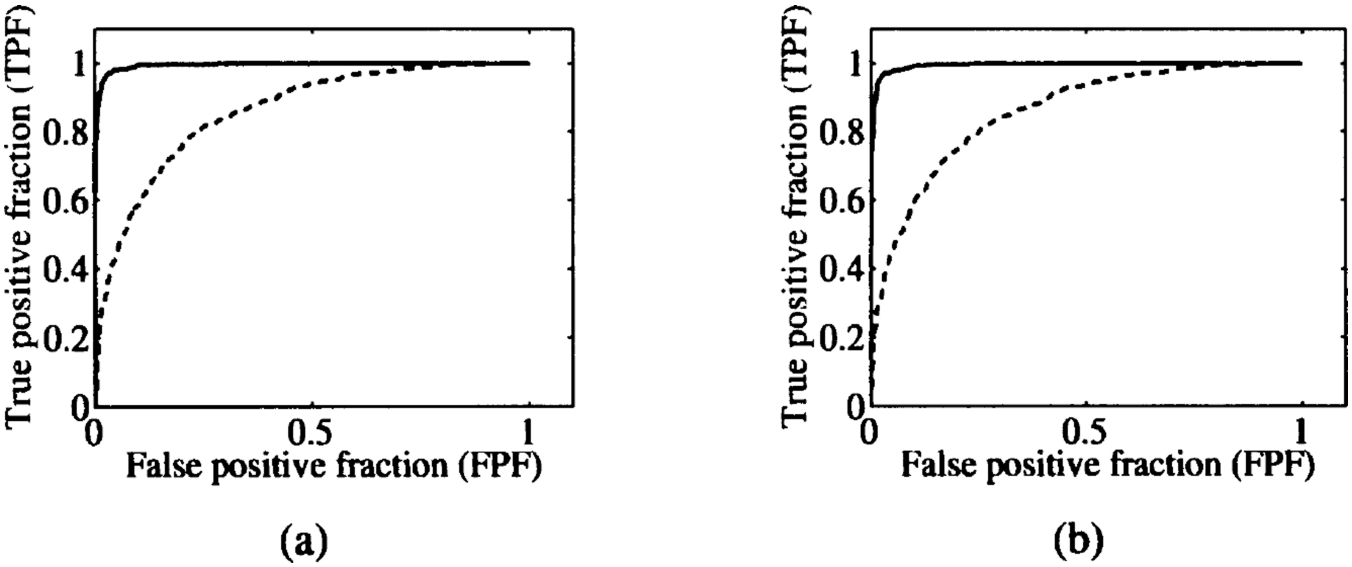

Fig. 5.

ROC curves for the two channelized Hotelling observers with adaptation (solid curves) and without adaptation (dashed curves). (a): with DOG channels; (b): with SQR channels.

TABLE I

Estimated AUCs, Standard Deviations σ, and Δd_A^2 for Different Model Observers for the Adaptive and Non-Adaptive Systems

	With Adaptation		Without Adaptation		
Observer	**AUC**	**σ**	**AUC**	**σ**	Δd_A^2
CHO_{DOG}	0.9951	0.001045	0.8611	0.008029	10.9783
CHO_{SQR}	0.9949	0.001033	0.8600	0.008053	10.8653

IEEE Nucl Sci Symp Conf Rec (1997). Author manuscript; available in PMC 2016 January 14.

TABLE II

AUCS and Δd_A^2 for Different Human Observers for the Adaptive and Non-Adaptive Systems

Observer	$AUC_{adapt.}$	$AUC_{non\text{-}adapt.}$	Δd_A^2
A	0.7625	0.5775	0.9442
B	0.8600	0.6400	1.0209
C	0.7650	0.6400	0.5148